Magnetic Integration With Controllable Leakage Inductance and Unbalanced Current Suppression for CF DAB Converter Based on Single EE Core

Jing Guo, *Student Member, IEEE*, Hui Wang, Guo Xu, *Senior Member, IEEE*, Yao Sun, *Member, IEEE*, and Mei Su, *Member, IEEE*

***Abstract*—A magnetic integrated structure based on single EE core (SEEC) is proposed to integrate all magnetic elements in current-fed dual active bridge (CF DAB) converter to improve power density. Different from previous works, all magnetic components of CF DAB, including two dc inductors, a transformer and a leakage inductance, are integrated in a SEEC. Moreover, the parameters of inductances and turns ratio can be accurately controlled by designing the number of winding turns and the air gap length. Furthermore, the unbalanced current suppression performance of the two interleaved dc inductors for CF DAB is improved due to the natural negative coupling between the two outer leg windings of the SEEC. In addition, based on the SEEC structure, an SEEC DAB converter is derived. Finally, the validity of the proposed solutions is verified by simulated results from Maxwell finite-element analysis and experimental results from a 1-kW laboratory prototype. Compared with CF DAB, the power density and efficiency are improved by 71% and 2.14%, respectively.**

***Index Terms*—Current-fed dual active bridge (CF DAB), controllable leakage inductance integration, single EE core (SEEC), unbalanced current suppression.**

I. Introduction

CURRENT-FED dual active bridge (CF DAB) converter has been a popular topology due to low input current ripple, wide voltage gain range and high efficiency [1], [2]. The topology of the CF DAB converter with paralleled branch is depicted in Fig. 1. Paralleled branch, consisting two dc inductors, are suitable for wide input voltage and high input current applications, such as energy storage systems, sustainable energy power system, electric vehicles, etc. [3], [4].

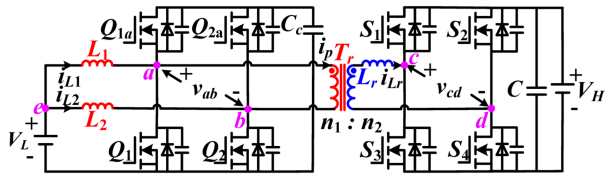

Fig. 1. Circuit diagram of CF-DAB converter.

In view of magnetic components, generally, four magnetics including two dc inductors, one leakage inductance and one transformer are needed, which somehow results in relatively low power density. To achieve high power density and high efficiency, magnetic integration, to sharing magnetic path and decrease the number of magnetic components, has been an attractive solution [5], [6], [7], [8], [9]. From the perspective of magnetic integration, the integration of multiple magnetic components can be viewed as the design of multiwinding coupled inductors, which is mainly divided into two categories: improvement of single magnetic structure [5], [6], [7], [8], [9], [10], [11] and combination of multiple magnetic structure [12], [13], [14], [15]. Improvement of single magnetic structure involves optimizing the design of multi-winding coupled inductors using a single magnetic core. For example, in [5] and [6], the two dc inductors on the low voltage side (LVS) are decoupled integrated. The number of magnetic components is reduced by the use of a coupled inductor instead of two discrete dc inductors. Han et al. [11] proposes a three-winding-coupled-inductor-based DAB (TWCI DAB) converter, which integrates two equivalent dc inductors and a high-frequency transformer into a three-winding-coupled-inductor (TWCI). Their advantages include minimizing the number of magnetic cores and maximizing window utilization, while the disadvantage is that the complexity of integrated structure design and production significantly increases as the number of windings increases. In addition, the combination of multiple magnetic structures, based on the combination of multiple two-phase coupled inductors, is a typical approach to realize the structure design of multi-winding coupled inductors. For example, Wang et al. [13] and Hu et al. [14] propose an interleaved coupled inductor DAB converter to integrate two dc inductors and a high-frequency transformer by

Received 28 October 2024; revised 5 February 2025; accepted 20 May 2025. Date of publication 9 June 2025; date of current version 5 August 2025. This work was supported in part by the National Natural Science Foundation of China under Grant 62125308, Grant U24A20157, Grant 62173351, in part by the JieBang Headed Program of Hunan Province under Grant 2021GK1250, in part by the Fundamental Research Funds in the Central South University under Grant 1053320231099, and in part by the 1st Doctoral Student Special Plan of the Young Elite Scientists Sponsorship Program by China Association for Science and Technology. Recommended for publication by Associate Editor N. R. Zargari. *(Corresponding authors: Hui Wang; Guo Xu.)*

Jing Guo, Hui Wang, Guo Xu, Yao Sun, and Mei Su are with the School of Automation, Central South University, Changsha 410083, China, and also with the Hunan Provincial Key Laboratory of Power Electronics Equipment and Grid, Changsha 410083, China (e-mail: guojingcsu@csu.edu.cn; wanghuicp9@csu.edu.cn; xuguocsu@csu.edu.cn; yaosun@csu.edu.cn; sumeicsu@csu.edu.cn).

Color versions of one or more figures in this article are available at https://doi.org/10.1109/TPEL.2025.3578034.

Digital Object Identifier 10.1109/TPEL.2025.3578034

combining two coupled inductors. To further improve the power density, leakage inductance is integrated into the dual coupled inductor in [15]. The design of the magnetic components is simplified due to the unit transformer power capacity is reduced. However, the potential increase in the number of magnetic cores, and as each unit transformer depends on the winding series, resulting in increased leakage flux. It should be noted that large leakage inductance will impact the power transmission and the soft switching performance of the CF DAB converter [4]. In fact, in addition to [15], the work in [5], [6], [7], [8], [9], [10], [11], [12], [13], and [14] need addition inductor to get the required leakage inductance to achieve power transmission and soft switching requirements.

On the other hand, the mismatching between the two dc inductor values, caused by manufacturing tolerance and termination configuration, etc., could lead to unbalanced current for the two dc inductors (L_1 and L_2 shown in Fig. 1) [16]. Recent studies have proved that coupled inductor (with a coupling coefficient not equal to zero) is an effective solution to unbalanced current suppression problem for pulsewidth modulation converters [17]. However, coupled inductors and transformers are usually designed separately, the leakage inductance is obtained through adding additional inductor [17], [18], [19]. Consequently, the component number for the solution with unbalanced current suppression is still large. In addition, from the perspective of the coupled mode of the magnetic integration, the aforementioned works are based on the decoupled integration design of two dc inductors [5], [6], [7], [8], [9], [10], [11], [12], [13], [14], [15]. Although the magnetic number is reduced by integrating multiple magnetic components in [5], [6], [7], [8], [9], [10], [11], [12], [13], [14], and [15], in fact, the two dc inductors are completely decoupled, making it difficult to guarantee unbalanced current suppression performance when the inductance parameters are different.

As mentioned above, the two goals of magnetic component integration and dc inductor unbalanced current suppression are independent and difficult to be compatible for the previous research. To solve this issue, a novel magnetic integrated structure based on single EE core (SEEC) is proposed in this article, that not only integrates all magnetic components in CF DAB converter with an SEEC, but also naturally has the function of dc inductor unbalanced current suppression. Some of the key advantages of the proposed solution are as follows:

1) Compared with the discrete magnetic components in CF DAB converter in [4], the SEEC integrates the two dc inductors, high frequency transformer and leakage inductance into a single standard EE core. In addition, unlike the TWCI DAB converter in [11], the leakage inductance and transformer turn ratio can be flexibly controlled by the designing the number of windings and the air gap length.
2) Due to the air gap in the center leg of the SEEC structure, a natural coupling relationship exists between the two windings on the outer legs. Therefore, compared with the unbalanced current of CF DAB converter in [4] caused by mismatched dc inductor values, the unbalanced current can be naturally suppressed by the two side windings of SEEC.

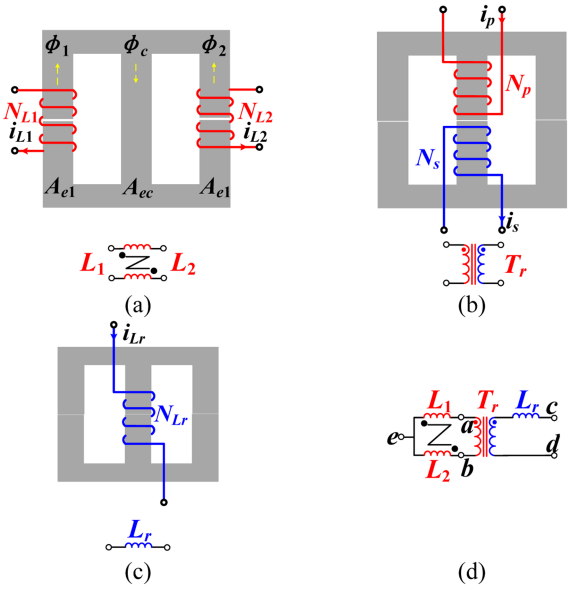

Fig. 2. CF-DAB converter with coupled inductor. (a) Coupled inductor. (b) High frequency transformer. (c) External series leakage inductance. (d) Circuit diagram.

3) Based on the SEEC structure, an SEEC DAB converter is derived. The SEEC DAB converter offers similar performance to the CF DAB converter, with small input current ripple and a wide voltage gain range, but uses only one magnetic component.

The rest of this article is organized as follows. The derived process of SEEC structure and SEEC DAB converter topology are descripted in Section II. In Section III, the analysis and design consideration of SEEC structure are discussed in detail. Section IV illustrates the simulation and experimental results to verify the effectiveness of the proposed solution. Finally, Section V concludes this article.

II. SEEC Structure and Converter Topology

A. Derivation Process of the Proposed SEEC Structure

The derivation process of the proposed SEEC as follows: to reduce the number of magnetic components, first, the coupled inductor (the coupling coefficient is equal to zero) can be applied to two dc inductors. Therefore, three EE cores are adopted for the coupled inductor, transformer and leakage inductance, as shown in Fig. 2. N_{L1} and N_{L2} represent the number of winding turns for two discrete dc inductors, and $N_{L1} = N_{L2}$. As Fig. 2(a) shown, the air gap is configured on the two outer legs and no air gap in center leg. In Fig. 2(b), N_p and N_s represent the number of primary and secondary winding turns of the transformer, respectively. N_{Lr} represents the number of winding turns for leakage inductance in Fig. 2(c). The circuit connection of the magnetic elements in Fig. 2(a), (b), and (c) is shown in Fig. 2(d).

Second, for further magnetic integration, one method is to integrate the transformer in Fig. 2(b) into the coupled inductor in Fig. 2(a), which is shown in Fig. 3(a). As shown in Fig. 3(a), the two windings on the outer legs function as the dc inductors

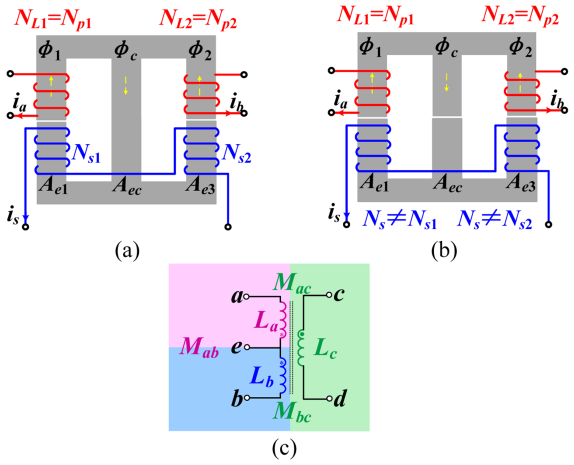

Fig. 3. Proposed magnetic integration structure based on single EE core (SEEC). (a) Magnetic core structure with no integrated leakage inductance. (b) Magnetic core structure with air gap of center leg to integrate leakage inductance. (c) The Circuit of the SEEC.

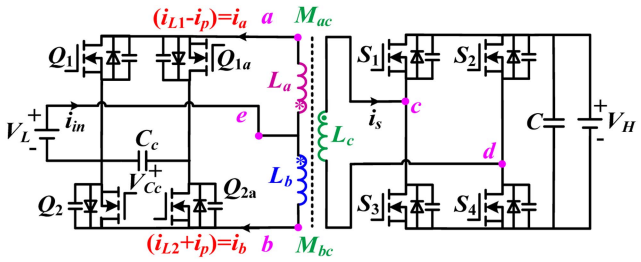

Fig. 4. Proposed SEEC DAB converter.

as well as the transformer primary windings. That is $N_{L1} = N_{p1}$ and $N_{L2} = N_{p2}$. N_{p1} and N_{p2} are the number of primary winding turns, and $N_{p1} = N_{p2}$. Additionally, N_{s1} and N_{s2} are the number of secondary winding turns, and $N_s = N_{s1} + N_{s2}$. Compared with coupled inductor in Fig. 2(a), the integrated magnetic structure in Fig. 3(a) initially successfully integrates the coupled inductor and one transformer.

Third, an air gap can be added in the center leg of the magnetic core in Fig. 3(a), which provides a flow path for the leakage flux, making the integration of leakage inductance possible, as shown in Fig. 3(b). It is worth noting there is a natural coupling relationship between the two windings on the outer legs due to the air gap of the center leg. From the winding current relationship, the integrated structure in Fig. 3(b) forms a three-winding coupled inductor model, whose circuit is drawn in Fig. 3(c).

B. Derived SEEC DAB Converter

According to the derivation process of the SEEC structure in Section II-A, one standard EE cores in Fig. 3(b) can function as the discrete magnetic elements in Fig. 1, that is the electrical circuit in Fig. 3(c) can equivalent to the circuit in Fig. 2(d). Therefore, the proposed SEEC DAB converter can be obtained, which is shown in Fig. 4.

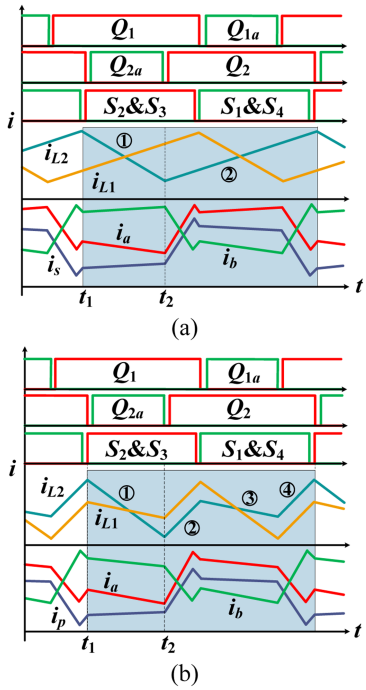

Fig. 5. Current waveforms of windings. (a) Current waveforms of decoupled integrated structure. (b) Current waveforms of the proposed SEEC.

The SEEC DAB converter can be equivalent to the CF DAB converter, then, it has small input ripple and wide voltage gain range. In addition, the traditional sense of leakage inductance and dc inductances can be controllable integrated into transformer, therefore, the number of magnetic elements is even least, the efficiency and power density can be improved. Meanwhile, the operation principle of SEEC DAB converter is similar as the CF DAB converter, under the pulsewidth modulation (PWM) plus phase shift (PPS) modulation, reference can be made to the working modes, power transmission and zero-voltage switching (ZVS) analysis in [4].

III. Analysis and Design Considerations

A. Analysis for Proposed SEEC Structure

As shown in Fig. 3(b), the proposed magnetic integrated structure SEEC is composed of an SEEC. Compare with the previous works, the number of magnetic components can be reduced to one for the proposed integrated solution.

In addition, when the two windings on the outer legs are designed to be negatively coupled, it is beneficial to improve the unbalanced current suppression performance [17], [18], [19]. As shown in Fig. 5, the top three waveforms are the switches gate control timing waveforms, including the driving pulses of Q_{1a}&Q_1, Q_{2a}&Q_2 and S_1–S_4. Due to the negative coupled coefficient, the current i_{L1} and i_{L2} flowing through the two dc inductors change from a two-stage triangular waveform to a four-stage waveform in one switching cycle, and the currents i_a and i_b flowing through both outer leg windings change from zero slope to negative slope at the t_1–t_2 stage. i_a and i_b are the

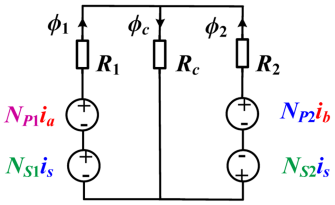

Fig. 6. Reluctance model of SEEC.

superposition of the dc inductor current i_{L1}, i_{L2} and the primary winding current i_p of the transformer, respectively. That are $i_a = i_{L1} - i_p$, $i_b = i_{L2} + i_p$. Therefore, both magnetic component integration and unbalanced current suppression performance of the CF DAB converter can be improved at the same time under SEEC.

According to the SEEC structure in Fig. 3(b), the reluctance model is represented in Fig. 6. The core reluctance is ignored since it is rather small compared with the air gap. Therefore, the magnetic fluxes can be calculated as (1).

Then, based on Faraday's law and (1), the inductance matrix of SEEC can be obtained as (2).

The transformer parameters of extended cantilever model can be derived according to [20] and expressed as (3)

$$\begin{cases} \phi_1 = \frac{N_{p1}i_a(R_2+R_c)-N_{p2}i_bR_c+N_{s1}i_b(R_2+R_c)+N_{s2}i_sR_c}{R_1R_2+R_1R_c+R_2R_c} \\ \phi_c = \frac{N_{p1}i_aR_2+N_{p2}i_bR_1+N_{s1}i_sR_2-N_{s2}i_sR_1}{R_1R_2+R_1R_c+R_2R_c} \\ \phi_2 = \frac{N_{p1}i_aR_c-N_{p2}i_b(R_1+R_c)+N_{s1}i_sR_c+N_{s2}i_s(R_1+R_c)}{R_1R_2+R_1R_c+R_2R_c} \end{cases} \tag{1}$$

$$\begin{cases} L_a = \frac{{N_{p1}}^2(R_2+R_c)}{R_1R_2+R_1R_c+R_2R_c} \\ L_b = \frac{{N_{p2}}^2(R_1+R_c)}{R_1R_2+R_1R_c+R_2R_c} \\ L_c = \frac{{N_{s1}}^2R_2+{N_{s2}}^2R_1+(N_{s1}+N_{s2})^2R_c}{R_1R_2+R_1R_c+R_2R_c} \\ M_{ab} = \frac{-N_{p1}N_{p2}R_c}{R_1R_2+R_1R_c+R_2R_c} \\ M_{ac} = \frac{N_{p1}[N_{s1}(R_2+R_c)+N_{s2}R_c]}{R_1R_2+R_1R_c+R_2R_c} \\ M_{bc} = \frac{-N_{p2}[N_{s2}(R_1+R_c)+N_{s1}R_c]}{R_1R_2+R_1R_c+R_2R_c} \end{cases} \tag{2}$$

$$\begin{cases} L_{m1} = L_1 = L_a = {N_{p1}}^2(R_2+R_c)/\Delta R \\ L_{m2} = L_2 = L_b = {N_{p2}}^2(R_1+R_c)/\Delta R \\ n_{E1} = N_s : N_p = \frac{M_{ac}}{L_a} = \frac{N_{s1}(R_2+R_c)+N_{s2}R_c}{N_{p1}(R_2+R_c)} \\ n_{E2} = N_s : N_p = \frac{M_{bc}}{L_b} = \frac{N_{s1}R_c+N_{s2}(R_1+R_c)}{N_{p2}(R_1+R_c)} \\ L_{r\_ab} = L_r = \left(L_c - \frac{M_{ac}^2}{L_a}\right) \| \left(L_c - \frac{M_{bc}^2}{L_b}\right) \end{cases} \tag{3}$$

where L_{m1} and L_{m2} are the equivalent magnetizing inductance of winding N_{p1} and N_{p2}, respectively. $N_p : N_s$ is the equivalent turns ratio of the transformer. L_{r_ab} is the equivalent leakage inductance. It should be noted that the equivalent magnetizing inductance is used as the dc inductance. According to (2) and (3), dc inductors, leakage inductance and the transformer turns ratio are related to the number of winding turns and reluctances. Therefore, the inductances and turns ratio can be flexibly controlled with the winding turns and air gap length of SEEC. It is worth noting that the proposed integrated solution can be extended to other topologies with inductances and transformer connection similar to CF DAB, such as current-fed resonant converters and current double rectifier converters.

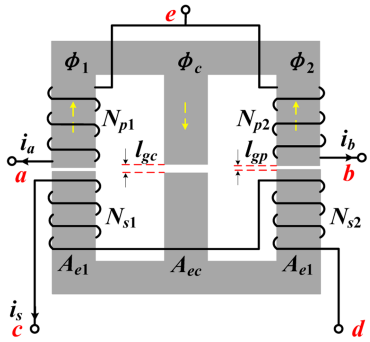

Fig. 7. Physical topology of SEEC using EE cores.

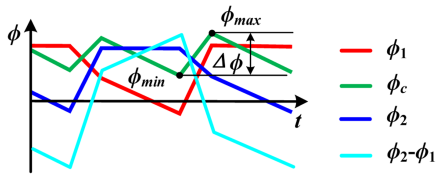

Fig. 8. Magnetic flux waveforms of SEEC.

B. SEEC Design Considerations

The physical topology of SEEC is shown in Fig. 7. The standard EE cores and the Litz wire windings constitute the SEEC structure. According to Fig. 3(b), the two windings N_{p1} and N_{p2} on the outer legs function as the dc inductors as well as the transformer primary windings. It can not only reduce the volume of the magnetic element, but also reduce the input current ripple. In addition, the air gap of center leg is used to integrate leakage inductor as well as naturally improve the performance of unbalanced current suppression. The two windings N_{s1} and N_{s2} of the outer legs can be used as the transformer secondary winding.

For the proposed SEEC, parameters including the turn numbers of the windings N_{p1}, N_{p2}, N_{s1}, N_{s2} and the core reluctance R_p ($R_1 = R_2 = R_p$), R_c need to be determined. The detailed design process of SEEC is as follows.

Step 1: Before calculating the core reluctance R_p, R_c and the numbers of the windings N_{p1}, N_{p2}, N_{s1}, N_{s2}, the transformer parameters, including L_{m1}, L_{m2}, L_{r_ab}, n_{E1}, n_{E2} and the coupled coefficient k of the two outer legs windings should be given. Then, according to (3), the core reluctance R_p, R_c and the numbers of the windings N_{p1}, N_{p2}, N_{s1}, N_{s2} can be calculated.

Step 2: To determine A_e of EE core, the max magnetic flux ϕ_{max} should be calculated. The magnetic flux can be calculated according to (1). The magnetic flux waveforms can be obtained, as shown in Fig. 8. As shown in Fig. 8, ϕ_1, ϕ_2, and ϕ_c are flux generated by the windings of two outer legs and center leg, respectively. It should be noted that the $\phi_2 - \phi_1$ is ac flux with no dc bias which flowing in two outer legs.

Step 3: To select the type of standard EE core, the A_e should be determined. A_e can be calculated as

$$A_e = \frac{\phi_{\max}}{B_{\text{recommend}}}. \tag{4}$$

TABLE I
COMPARISON OF DIFFERENT MAGNETIC PARTS DESIGNS

Magnetic category	discrete magnetics in CF-DAB			TWCI DAB		SEEC DAB
	transformer design	2×inductor design	leakage design	TWCI	leakage design	SEEC
Core material	Mn-Zn power ferrite DMR40					
Core model	PQ40	C055071A2	RM12	EE42	RM12	EE42
Length (mm)	40	2×81.4	37.6	42	37.6	42
Width (mm)	28	2×32.8	16.1	20	16.1	20
Height (mm)	40	2×10.7	24.6	42	24.6	42
Magnetic flux density change (T)	ΔB=0.15					
Effective *Ve* (mm^3)	19698	2×5340	8322	22601	8322	22601
Effective *Ae* (mm^2)	210	65.6	146	233	146	233
Turns	$N_1 : N_2$ =5 :25	2×5	18	$N_p : N_s$= 5 : 25	18	N_{p1}:N_{p2}: N_{s1}:N_{s2} =5 : 5: 22 : 10
Power density (W/in^3)	424			530		725
Number of magnetics	4			2		1

B_{recommed} can be recommended according to the operating frequency of the converter.

Step 4: After selecting the type of standard EE core, the air gap length l_{gp} and l_{gc} of the magnetic core can be calculated as

$$l_{gp} = R_p \mu_0 A_{e1}, \quad l_{gc} = R_c \mu_0 A_{ec} \tag{5}$$

where μ_0 is space permeability.

C. Design and Loss Breakdown Comparison Between SEEC DAB and CF DAB

The design parameters for comparison of proposed SEEC, TWCI in [11], and discrete magnetics of CF DAB in [4] are given in Table I. To ensure a fair comparison, all devices and PCBs remain consistent, with the exception of the magnetic components. Moreover, core types are selected to maintain alike changes in magnetic flux density. As given in Table I, the proposed SEEC structure, employing an SEEC manages to reduce the number and occupied volume of the magnetic core while achieving higher power density. In comparison to TWCI in [11] and the discrete magnetic of CF DAB in [4], the power density has been increased by 36.8% and 71%, respectively. Moreover, the number of magnetic components can be reduced to 1 with the proposed SEEC.

The loss breakdown comparisons between the discrete magnetics case of CF DAB and the proposed SEEC DAB at different V_L ($V_L = 18$ V, 27 V and 36 V) and different loads ($P = 100$ and 1000 W) are shown in Fig. 9. $P_{\text{SEEC\_DAB}}$ and $P_{\text{CF\_DAB}}$ are total losses of SEEC DAB converter and CF DAB converter, respectively. $P_{\text{SEEC\_copper}}$ and $P_{\text{SEEC\_core}}$ are copper loss and core loss of the SEEC DAB converter, respectively. P_{Ldc_copper} and P_{Ldc_core} are copper loss and core loss of the two dc inductors in CF DAB converter, respectively. P_{T_copper} and P_{T_core} are copper loss and core loss of the transformer in CF-DAB converter, respectively. P_{Lr_copper} and P_{Lr_core} are copper loss and core loss of the leakage inductor in CF-DAB converter, respectively. $P_{\text{turn-on}}$ and $P_{\text{turn-off}}$ are turn-ON loss and turn-OFF loss of all the switches, respectively. P_{con} is conduction loss for switches. P_{dri} is driving loss.

Under the PWM modulation strategy, the driving signals for the two switches in any bridge are complementary. The conduction of the antiparallel diode only exists in the dead time, and it lasts for a very short time. Thus, the conduction loss of antiparallel diode is ignored in this article to simplify the analysis. Except for the difference of two dc inductors, transformer and leakage inductor, other experimental parameters are the same, such as MOSFETs, PCB circuit boards, etc. In SEEC DAB, all the MOSFETs are turned on with ZVS. Hence, the turn-ON losses are zero. The total losses consist of three parts, namely driving loss, switches loss, and SEEC loss. As shown in Fig. 9(a), when the converter works at $V_L = 18$ V and light load (100 W), the total loss of CF DAB is higher than that of the proposed SEEC DAB about 5.5 W, which is mainly caused by hard turning off loss, leading to low efficiency at light load. When $V_L = 36$ V, the difference is reduced to 3.6 W. As the input voltage increases, the current decreases, then the turn-OFF loss and the copper loss of the magnetic elements decrease. As shown in Fig. 9(b), when the converter works at $V_L = 18$ V and heavy load condition (1000 W), the power loss with the proposed CF DAB is higher than that of SEEC DAB about 16.8 W, which is mainly caused by the increased core and copper losses. It should be noted that the winding loss and core loss are based on the results calculated by the Dowell one-dimensional ac resistance model [21] and the theory of Steinmetz Equation [22]. In addition, due to the smaller air gap length, the impact of the air gap edge diffusion flux for the winding eddy current loss in SEEC can be ignored. However, the impact of the longer air gap length cannot be ignored. Consider the difficult of the realize of magnetic components, especially the integrated structure, when the winding position is moved, the

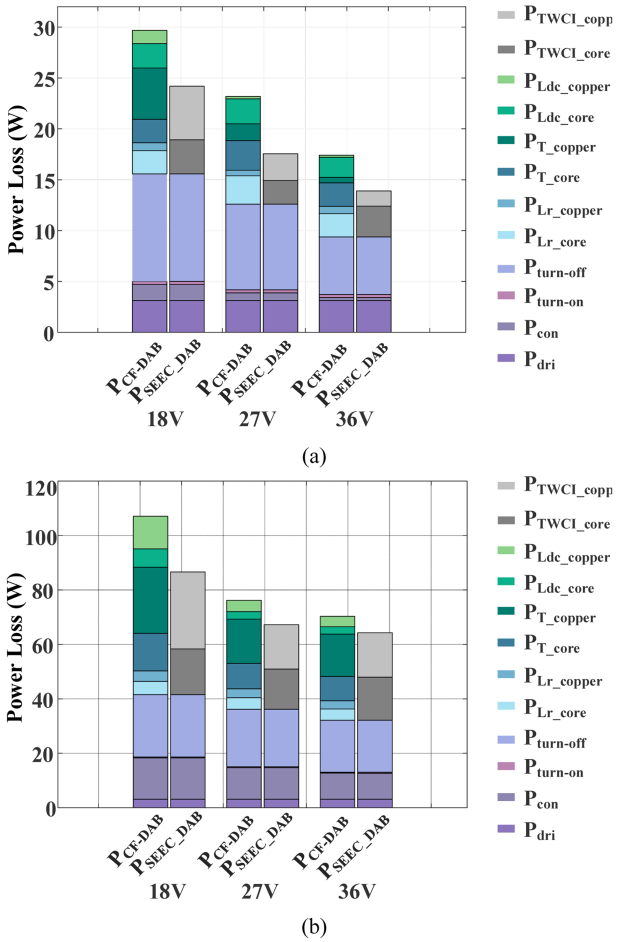

Fig. 9. Loss breakdown at different V_L and different loads. (a) At light load ($P = 100$ W). (b) At full load ($P = 1000$ W).

limited window size is a challenge. Therefore, the optimization design of the air gap location is an issue worthy of further study in the future.

At low input voltages condition, the conduction time and input current increases as the input voltage decreases. The corresponding switching loss and magnetic element loss increase. Magnetic element loss and hard turn OFF loss dominate at light loads, leading to low efficiency at light load. As can be seen, the total loss of the integrated magnetic SEEC is reduced according to Fig. 9. Therefore, SEEC DAB efficiency is higher than CF DAB.

In addition to the benefits of unbalanced current suppression improvement, the inductances and turns ratio can be flexibly controlled with the winding turns and air gap length of single standard EE core under the proposed SEEC. In addition, according to Table I, when transmitting the same power, the power density of SEEC DAB can also be increased due to the reduction of core number and volume. Furthermore, loss of SEEC DAB is less than CF DAB with discrete magnetics according to the loss breakdown.

IV. Simulation and Experimental Verification

In order to verify the proposed SEEC structure and SEEC DAB converter, the Maxwell 2D finite-element analysis (FEA) is investigated to obtained the inductance matrix and the flux distribution of SEEC. In addition, the experimental results of SEEC DAB converter are shown, including the performance of unbalanced current suppression, dynamic response, the comparison of operation efficiency between CF DAB converter and SEEC DAB converter. The SEEC DAB converter experimental prototype and the discrete magnetic components are built, as shown in Fig. 10.

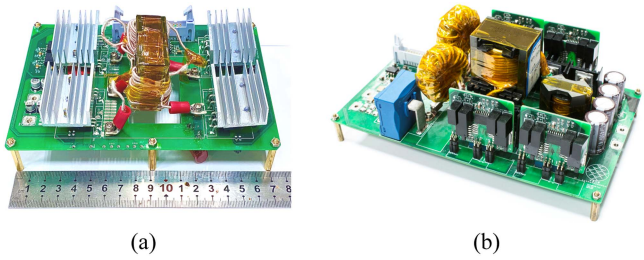

Fig. 10. Experimental prototype. (a) Experimental prototype of proposed SEEC DAB converter. (b) The experimental prototype of CF DAB converter.

TABLE II
System Specifications

P	1 kW	L_r	15 μH
f	150 kHz	L_1/L_2	9 μH
V_L	18–36 V	$N_p : N_s$	3:10
V_H	240 V	C_c	60 μF
Q_1, Q_2, Q_{1a}, Q_{2a}	IPP023N10N5	S_1-S_4	UJ3C065030K3S

The system parameters are given in Table II. As shown, input voltage is 18–36 V and output voltage is 240 V, rated power is 1 kW, switching frequency is 150 kHz, turns ratio of transformer N_p:$N_s = 3/10$, clamping capacitor $C_c = 60\,\mu$F. Taking the ZVS design, current ripple, and RMS current into consideration, the dc inductors L_1 and L_2 are designed to be 9 μH. Based on considering the ZVS range, maximum power transfers capability and the RMS current, the leakage inductance $L_r = 15\,\mu$H is finally selected. According to the voltage, current stresses and margin should be considered, device type IPP023N10N5 from Infineon company is selected for the LVS switches, and device type UJ3C065030K3S from United-SiC company is selected for the high voltage side (HVS) switches.

In this article, the magnetic core of EE42 DMR95 is selected. The coupled coefficient of the two outer legs windings is -0.7 to make a tradeoff between the unbalanced current suppression performance of the paralleled branch and the leakage inductance integration effect. According to (2) and (3) in the revised manuscript, the related parameters of the core are as follow, $N_{p1} = 5$, $N_{p2} = 5$, $N_{s1} = 22$, $N_{s2} = 10$, $l_{gp} = 0.289$ mm, $l_{gc} = 0.45$ mm. The parameters of SEEC are given in Table III.

A. Simulation Results

The flux distribution in Maxwell FEA of SEEC is shown in Fig. 11. As seen, the max flux density $B_{\max}$ is less than 0.15T. In addition, the number of winding turns on both sides is unevenly distributed to produce controllable leakage inductance,

TABLE III
PARAMETERS OF SEEC

Item	Value	Item	Value
l_{gp}	0.289 mm	l_{gc}	0.45 mm
N_{P1}	5	N_{S1}	22
N_{P2}	5	N_{S2}	10

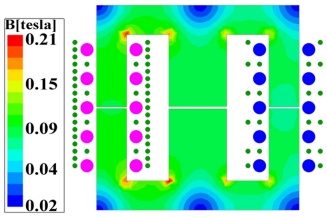

Fig. 11. Flux distribution of SEEC in Maxwell FEA.

TABLE IV
COMPARISONS OF THE INDUCTANCE MATRIX

Item	Theoretical results	Simulated results	Measured results
L_a (μH)	9	9.1(↑1.11%)	8.76(↓2.6%)
L_b (μH)	9	9.1(↑1.11%)	9.16(↑1.18%)
L_c (μH)	293	287.5(↓1.9%)	296.8(↑1.3%)
M_{ab} (μH)	-4.2	-4.08(↓2.8%)	-4.41(↑5%)
M_{ac} (μH)	50	51.35(↑2.7%)	48.9(↓2.2%)
M_{bc} (μH)	-50	-51.35(↑2.7%)	-53.4(↑2.7%)

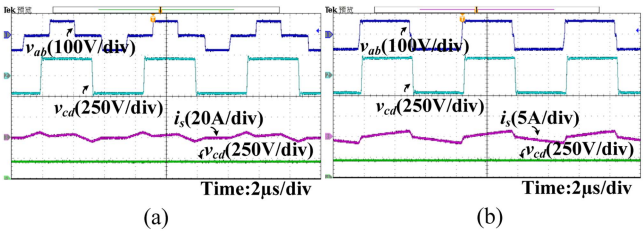

Fig. 12. Steady-state waveforms under light load. (a) Under the input voltage $V_L = 18$ V. (b) Under the input voltage $V_L = 36$ V.

although the distribution of flux is not uniform, conform to safety specifications. The comparisons among the theoretical results, simulated results, and measured results of inductance matrix are given in Table IV. As seen, the simulated results and measured results are very closed to the theoretical results.

B. Experimental Results

In order to verify the proposed SEEC magnetic integrated structure and SEEC DAB converter, the steady-state operation and soft-switching of switches under different input voltages and different loads are shown.

Figs. 12 and 13 show the steady-state waveforms of the proposed SEEC DAB in boost mode under different voltages and loads. Fig. 12(a) and (b) describes the steady-state waveforms at light load with $V_L = 18$ and $V_L = 36$ V, respectively. It is seen that the pulsewidth of the midpoint voltage v_{cd} between

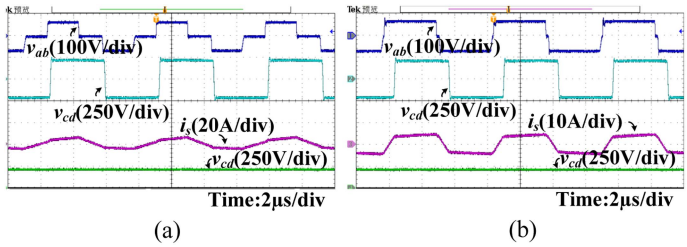

Fig. 13. Steady-state waveforms under full load. (a) Under the input voltage $V_L = 18$ V. (b) Under the input voltage $V_L = 36$ V.

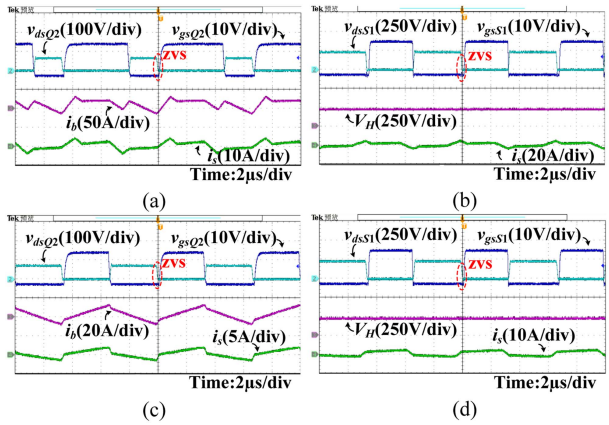

Fig. 14. Soft-switching waveforms of switches with light load. (a) Q_2 when $V_L = 18$ V. (b) S_1 when $V_L = 18$ V. (c) Q_2 when $V_L = 36$ V. (d) S_1 when $V_L = 36$ V.

the HVS bridges is always fixed at 0.5 in these figures, which means the duty cycle of HVS switches is always equal to 0.5. The waveforms of the LVS voltage v_{ab} are similar when $d > 0.5$. When $d = 0.5$, the operation waveforms of the PPS control is exactly the same as an SPS controlled converter. In addition, v_{cd} lags behind v_{ab} in phase to adjust the power among all waveforms. Similarly, Fig. 13(a) and (b) depicts steady-state waveforms at full load. These demonstrate the working principle of the proposed SEEC DAB. It is clear that the experimental waveforms coincide with the theoretical analysis pretty well.

The ZVS experimental waveforms of switches are shown in Figs. 14 and 15. Compared to heavy load, it is most difficult to achieve ZVS under light load. Meanwhile, compared with the top switch Q_{1a} of LVS and the bottom switch Q_2 of LVS, S_1 of HVS are more difficult to realize ZVS. Consequently, Fig. 14 illustrates the ZVS experimental waveforms of the bottom switch Q_2 of LVS and switch S_1 of HVS under different voltages at light load. The results show that ZVS can be achieved despite the voltage fluctuations at light load. Fig. 15 illustrates the ZVS experimental waveforms of the bottom switch Q_2 of LVS and S_1 of HVS at different voltages at full load. It can be seen that ZVS can be achieved when input voltage changes.

In order to verify the unbalance current suppression performance of SEEC structure, Fig. 16 shows unbalanced current suppression waveforms under different input voltages and different loads of SEEC in the SEEC DAB converter. It should be noted that a 15% difference between the two inductor values

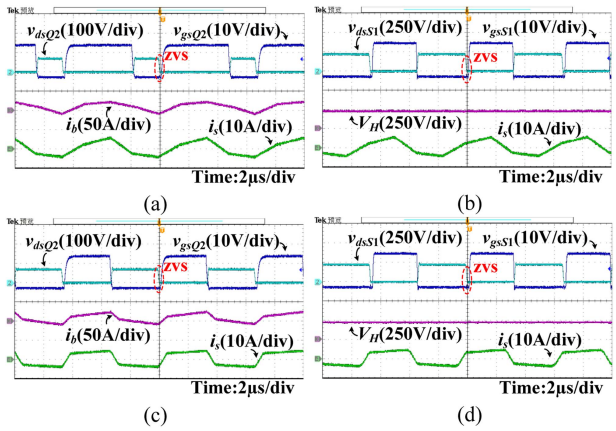

Fig. 15. Soft-switching waveforms of switches with full load. (a) Q_2 when $V_L = 18$ V. (b) S_1 when $V_L = 18$ V. (c) Q_2 when $V_L = 36$ V. (d) S_1 when $V_L = 36$ V.

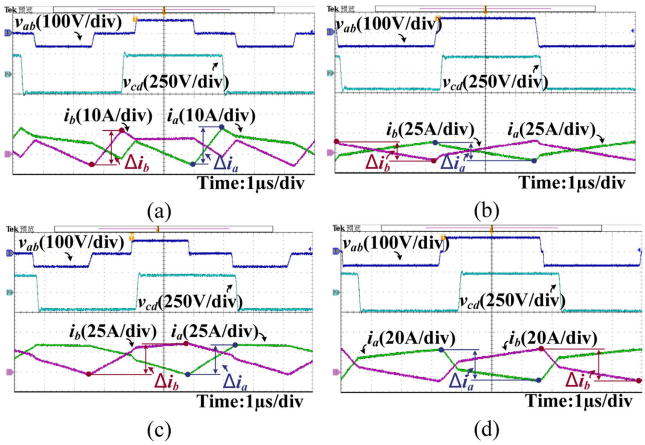

Fig. 16. Unbalanced current suppression performance with SEEC. (a) Light load when $V_L = 18$ V. (b) Light load when $V_L = 36$ V. (c) Full load when $V_L = 18$ V. (d) Full load when $V_L = 36$ V.

TABLE V
CURRENT RIPPLE OF SEEC DAB CONVERTER

Δi(A)	Δi_1	Δi_2	Δi_2 - Δi_1
Mode 1	18.1	19.4	1.3
Mode 2	25	26.8	1.8
Mode 3	34.9	37.1	2.2
Mode 4	29.5	31.4	1.9

Mode 1: Light load when $V_L = 18$ V; Mode 2: Light load when $V_L = 36$ V; Mode 3: Full load when $V_L = 18$ V; Mode 4: Full load when $V_L = 36$ V.

(L_a and L_b). For instance, in operation mode 1 under a light load with $V_L = 18$ V, as shown in Fig. 16(a), the difference between two current ripples Δi_1 and Δi_2 of the two outer leg windings is only 1.3 A with the SEEC structure. Therefore, the suppression rate of the unbalance current is effectively improved with the SEEC structure. All current ripple values for different operation modes are given in Table V. The suppression rates of other modes of unbalance current are similar to that of mode 1, as shown in Fig. 16(b), (c), and (d). It can be seen that, regardless of the load, the SEEC structure provides excellent unbalanced current suppression performance between the two outer legs windings.

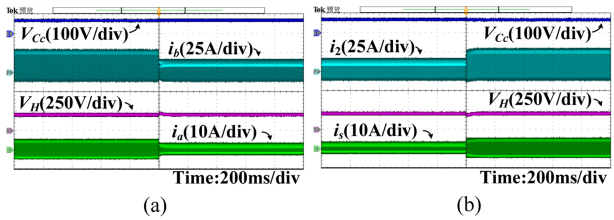

Fig. 17. Load-step experiment result. (a) Full load to half load when $V_L = 27$ V. (b) Half load to full load when $V_L = 27$ V.

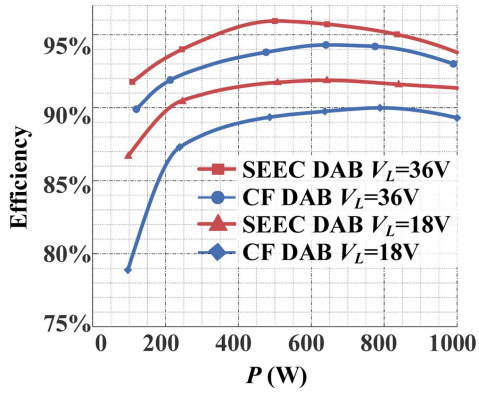

Fig. 18. Efficiency comparisons between the proposed SEEC DAB and CF DAB at different voltages and different loads.

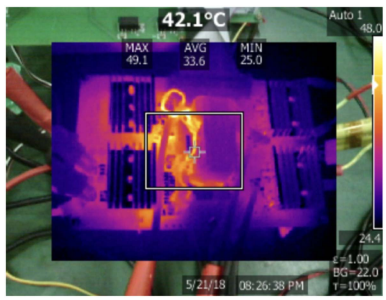

Fig. 19. Thermal distribution of the SEEC structure.

Fig. 17 illustrates the load-step experimental results of the proposed SEEC DAB converter with $V_L = 27$ V. Fig. 17(a) shows the load-step from full load to half load, and Fig. 17(b) shows the load-step from half load to full load, V_H can both keep stable and can both return to the steady-state value within 20 ms.

Fig. 18 shows the measured efficiency at different loads and different voltages. In order to verify the effectiveness of the SEEC DAB, the discrete magnetic case of CF-DAB is also measured. The overall conversion efficiency is high, and the highest efficiency of the SEEC DAB reaches 95.9%. The proposed SEEC DAB achieves 2.14% higher efficiency than the discrete magnetic elements of CF DAB with the same magnetic material. The power loss at light load can be reduced for SEEC DAB, because the core loss makes up the majority of the total loss when converter operates at light load condition.

Fig. 19 shows the thermal distribution of the SEEC structure. The prototype is operated at an ambient temperature of about

24 °C with a fan (speed 2500 r/min, air flow 25 CFM) for 1 hour until the temperature stabilizes. As seen, the temperature of the EE core is about 42 °C. And the highest temperature of core is 49.1 °C, which conforms to the design specifications.

V. Conclusion

In this article, a SEEC magnetic integrated structure is proposed. Compared with discrete magnetic components of CF DAB converter, two dc inductors, one leakage inductance and one high frequency transformer are integrated into a single standard EE core. The equivalent relationship between the proposed SEEC model and the extended cantilever model of three-ports transformer is analyzed in detail, the parameters of inductances and turns ratio can be controlled flexibly by adjusting winding turns and air gap length of the SEEC. Meanwhile, the unbalanced current suppression performance of the paralleled branch is improved due to the natural negative coupling between the two outer leg windings of the SEEC. Furthermore, based on the SEEC structure, a SEEC DAB converter is derived. The proposed SEEC DAB converter can realize ZVS for all switches in the full load range under the condition of wide input voltage variation with the adopted PWM modulation, similar to the TWCI DAB converter. In addition, a comparison of the design parameters and loss breakdown between the CF DAB converter and the SEEC DAB converter shows that the SEEC DAB achieves higher power density and significantly reduced losses. Finally, an FEA simulation model and an 18–36 V/240 V 1 kW SEEC DAB prototype are built, and experimental results confirm the effectiveness of the proposed solution.

References

[1] D. Sha, Y. Xu, J. Zhang, and Y. Yan, "Current-fed hybrid dual active bridge DC–DC converter for a fuel cell power conditioning system with reduced input current ripple," *IEEE Trans. Ind. Electron.*, vol. 64, no. 8, pp. 6628–6638, Aug. 2017.

[2] Z. Guo, K. Sun, T.-F. Wu, and C. Li, "An improved modulation scheme of current-fed bidirectional DC–DC converters for loss reduction," *IEEE Trans. Power Electron.*, vol. 33, no. 5, pp. 4441–4457, May 2018.

[3] D. Sha, X. Wang, and D. Chen, "High-efficiency current-fed dual active bridge DC–DC converter with ZVS achievement throughout full range of load using optimized switching patterns," *IEEE Trans. Power Electron.*, vol. 33, no. 2, pp. 1347–1357, Feb. 2018.

[4] J. Guo et al., "Design considerations for PPS controlled current-fed DAB converter to achieve full load range ZVS and low inductor current stress," *IEEE Trans. Ind. Appl.*, vol. 57, no. 6, pp. 6261–6276, Nov./Dec. 2021.

[5] D. Sha, K. L. X.Wang, and C. Chen, "A current-fed dual-active-bridge DC–DC converter using extended duty cycle control and magnetic-integrated inductors with optimized voltage mismatching control," *IEEE Trans. Power Electron.*, vol. 34, no. 1, pp. 462–473, Jan. 2019.

[6] C. Jiang and H. Liu, "A novel interleaved parallel bidirectional dual-active-bridge DC–DC converter with coupled inductor for more-electric aircraft," *IEEE Trans. Ind. Electron.*, vol. 68, no. 2, pp. 1759–1768, Feb. 2021.

[7] H. Bahrami, S. Farhangi, H. Iman-Eini, and E. Adib, "A new interleaved coupled-inductor nonisolated soft-switching bidirectional DC–DC converter with high voltage gain ratio," *IEEE Trans. Ind. Electron.*, vol. 65, no. 7, pp. 5529–5538, Jul. 2018.

[8] H. Bahrami, S. Farhangi, H. Iman-Eini, and E. Adib, "Analysis, design, and implementation of DC–DC IBBC-DAHB converter with voltage matching to improve efficiency," *IEEE Trans. Ind. Electron.*, vol. 66, no. 7, pp. 5209–5219, Jul. 2019.

[9] Z. Yan, J. Zeng, W. Lin, and J. Liu, "A novel interleaved nonisolated bidirectional DC–DC converter with high voltage-gain and full-range ZVS," *IEEE Trans. Power Electron.*, vol. 35, no. 7, pp. 7191–7203, Jul. 2020.

[10] R. Hu, J. Zeng, Z. Yu, Z. Yan, and J. Liu, "Secondary side cascaded winding-coupled bidirectional converter with wide ZVS range and high conversion gain," *IEEE J. Emerg. Sel. Topics Power Electron.*, vol. 9, no. 2, pp. 1444–1454, Apr. 2021.

[11] H. Han, J. Guo, G. Xu, J. Xu, D. Liu, and M. Su, "Three winding coupled inductor-based dual active bridge DC-DC converter with full load range ZVS under wide voltage range," *IEEE Trans. Ind. Electron.*, vol. 69, no. 7, pp. 6935–6947, Jul. 2022.

[12] X. Chen, X. G, Q. Shen, Y. Sun, and M. Su, "Magnetizing and leakage inductance integration for split transformers with standard UI cores," *IEEE Trans. Power Electron.*, vol. 37, no. 11, pp. 12980–12985, Nov. 2022.

[13] Z. Wang, C. Li, and Z. Zheng, "A high-step-up low-ripple and high-efficiency DC-DC converter for fuel-cell vehicles," *IEEE Trans. Power Electron.*, vol. 37, no. 3, pp. 3555–3569, Mar. 2022.

[14] R. Hu et al., "An interleaved bidirectional coupled-inductor based DC–DC converter with high conversion ratio for energy storage system," *IEEE Trans. Ind. Electron.*, vol. 69, no. 6, pp. 5648–5659, Jun. 2022.

[15] J. Guo, H. Wang, G. Xu, X. Li, Y. Sun, and M. Su, "Dual coupled inductors with controllable integrated leakage inductance and CM noise suppression for CF-DAB converter," *IEEE Trans. Power Electron.*, vol. 38, no. 7, pp. 8033–8038, Jul. 2023.

[16] M. Hadi, E. Nour, and A. M. Osama, "An integrated interleaved ultrahigh step-up DC–DC converter using dual cross-coupled inductors with built-In input current balancing for electric vehicles," *IEEE J. Emerg. Sel. Topics Power Electron.*, vol. 8, no. 1, pp. 644–657, Mar. 2020.

[17] Y. Zhang, R. Liu, and H. Wang, "Current balancing of a multiphase inverter for LCC-S compensated wireless power transfer system based on mutually negatively coupled inductors," *IEEE Trans. Power Electron.*, vol. 38, no. 10, pp. 12411–12415, Oct. 2023.

[18] S. Mao, Y. Chen, C. Li, X. Mao, and X. Chen, "A coupled-inductor-based LCC resonant converter with the primary-parallel–secondary-series configuration to achieve output-voltage sharing for HV generator applications," *IEEE Trans. Power Electron.*, vol. 34, no. 7, pp. 6512–6523, Jul. 2019.

[19] F. Li, L. Wang, M. Wu, and L. Yu, "A coupled-inductor-based input-parallel output-parallel quasi-resonant single-stage DC–DC converter to mitigate current difference," *IEEE Trans. Ind. Electron.*, vol. 71, no. 7, pp. 6108–6122, Jul. 2024.

[20] G. H. John, O. D. Neil, and G. E. Michael, "The extended T model of the multiwinding transformer," in *Proc. 3Wt Annu. IEEE Power Elecrronics Specinlisrs Conf.*, 2004, pp. 1817–1812.

[21] P. L. Dowell, "Effect of eddy currents in transformer windings," *IEE Proc*, vol. 113, no. 8, pp. 1387–1394, Aug. 1966.

[22] M. H. Ahmed, C. Fei, F. C. Lee, and Q. Li, "Single-stage high-efficiency 48/1 V sigma converter with integrated magnetics," *IEEE Trans. Ind. Electron.*, vol. 67, no. 1, pp. 192–202, Jan. 2020.

Jing Guo (Student Member, IEEE) was born in Shaanxi, China, in 1997. He received the B.S. degree in electrical engineering and automation from Zhejiang Sci-Tech University, Hangzhou, China, in 2019, the M.S. degree in electrical engineering in 2022 from Central South University, Changsha, China, where he is currently working toward the Ph.D. degree in control science and engineering.

His research interests include magnetic integration design and soft switching technology for bidirectional dc–dc converters.

Hui Wang received the B.S. degree in automation, the M.S. degree in electrical engineering, and the Ph.D. degree in control science and engineering from the Central South University, Changsha, China, in 2008, 2011, and 2014, respectively.

He is currently a Full Professor with the School of Automation, Central South University. His research interests include matrix converters, dc/dc converters, and solid-state transformers.

Guo Xu (Senior Member, IEEE) received the B.S. degree in electrical engineering and automation and the Ph.D. degree in control science and engineering from the Beijing Institute of Technology, Beijing, China, in 2012 and 2018, respectively.

From 2016 to 2017, he was a Visiting Student with the Center for Power Electronics System, Virginia Polytechnic Institute and State University, Blacksburg, VA, USA. Since 2018, he has been with the School of Automation, Central South University, Changsha, China, where he is currently an Associate Professor. His research interests include modeling and control of power electronics converters, high-efficiency power conversion, and magnetic integration in power converters.

Yao Sun (Member, IEEE) was born in Hunan, China, in 1981. He received the B.S., M.S. and Ph.D. degrees in control theory and control engineering from the Central South University, Changsha, China, in 2004, 2007 and 2010, respectively.

He is currently a Professor with the School of Automation, Central South University, China. His research interests include matrix converter, microgrid, and wind energy conversion system.

Mei Su (Member, IEEE) was born in Hunan, China, in 1967. She received the B.S., M.S. and Ph.D. degrees in control theory and control engineering from the School of Automation, Central South University, Changsha, China, in 1989, 1992 and 2005, respectively.

She is currently a Full Professor with the School of Automation, Central South University. Her research interests include matrix converter, adjustable speed drives, and wind energy conversion system.